Vibration-assisted installation and decommissioning of a slip-joint

Cabboi, Alessandro; Segeren, Maxim; Hendrikse, Hayo; Metrikine, Andrei

DOI
10.1016/j.engstruct.2019.109949

Publication date
2020

Document Version
Final published version

Published in
Engineering Structures

Citation (APA)
Cabboi, A., Segeren, M., Hendrikse, H., & Metrikine, A. (2020). Vibration-assisted installation and decommissioning of a slip-joint. *Engineering Structures*, *209*, Article 109949. https://doi.org/10.1016/j.engstruct.2019.109949

Engineering Structures 209 (2020) 109949

Contents lists available at ScienceDirect

Engineering Structures

journal homepage: www.elsevier.com/locate/engstruct

Vibration-assisted installation and decommissioning of a slip-joint

Alessandro Cabboi*, Maxim Segeren, Hayo Hendrikse, Andrei Metrikine

Faculty of Civil Engineering and Geosciences, Delft University of Technology, Stevinweg 1, 2628CN Delft, Netherlands

ARTICLE INFO

Keywords:
Jointed structures
Experimental dynamics
Friction
Wind turbine
Transition piece
Grouted connection

ABSTRACT

The structural failure of grouted connections for offshore wind turbines focused the industrial attention towards different and innovative solutions to guarantee a safe connection between the monopile foundation and the turbine tower. An alternative option to the traditional grouted joint is a direct steel-to-steel connection, also called a slip-joint which was sporadically used for onshore wind turbines. To such regard, a proof of concept is illustrated concerning a new installation and decommissioning technique of a slip-joint. The key aspect of the proposed method is to guarantee a proper fit and sound contact of the slip-joint by means of vibration-assisted settlements. Therefore, the effectiveness of applying a harmonic excitation during the installation and decommissioning procedure is experimentally investigated using a 1:10 scaled model of the slip-joint. During the dynamic tests, the applied static load and the settlements of the joint are monitored using load cells, displacement sensors and strain gauges placed both inside and outside the conical surfaces. For the installation tests, the results show that settlement occurs when applying a harmonic load at specific forcing frequencies. All the vibration-induced settlements tend to stabilize in time, indicating that a sound contact through vibration-assisted installation can be achieved. In a similar way, the decommissioning proved to be effective at certain forcing frequencies. According to all the tests performed during this experimental campaign, both the installation and decommissioning tests showed to be more sensitive to the forcing frequency rather than to the dynamic forcing amplitude.

1. Introduction

1.1. Slip-joint technology

In 2009, the fallacies of the design standards concerning the grouted connections between wind turbine tower and monopile foundation strikingly emerged: around 1000 structures were slowly sinking on their steel-concrete connection [1,2]. This unforeseen joint failure initiated a series of alarming consequences. One of the biggest concerns was the increasing risk of new stress hotspots which were not accounted for in the original design. Furthermore, if sliding would have persisted, access platforms would have inevitably moved into the wave splash zone increasing the risk of getting damaged during sea storms. A persisting settlement would have also reduced the turbine height, causing economic losses due to the decrease of power production. In order to prevent further damages, these structures were retrofitted with elastomeric bearings at a significantly high cost. Consequently, most of the research activities in that field focused on finding alternative solutions [3,4], understanding the factors that caused the unexpected failure of the grouted connection [5,6], and experimentally investigating the failure patterns for different loading conditions [7,8].

In 2011 [9], the DNV offshore standards have been updated as a result of several industrial projects aimed at improving the design of grouted connection. The main recommendations of the revision suggested the introduction of shear keys and the realization of a small cone angle in the grouted section between the monopile and the transition piece [10], see Fig. 1 for a schematic representation. Shear keys are circumferential weld beads located on the external side of the monopile and the inside of the transition piece, adding a slip-resistant mechanism to the grouted connection. Possible design practice for the shear keys have been investigated and are essentially based on non-linear finite element models [11,12]. As mentioned before, a slip-resistant mechanism can also be achieved by a conical grouted connection. The conical shape will introduce compressive contact stresses, initiating a frictional mechanism able to resist slipping between the grout and the steel [13]. Recent work further investigated the influence of the design parameters, such as steel wall thickness, cone angle and grout length, on the failure modes of a conical grouted connection [14] suggesting a probability-based design method.

An alternative solution to the grouted connection is the bolted flange connection between the monopile and the transition piece, see Fig. 1. The feasibility of the flanged connection was proven by the

---

* Corresponding author.
E-mail addresses: A.Cabboi@tudelft.nl, alexcabboi@gmail.com (A. Cabboi).

https://doi.org/10.1016/j.engstruct.2019.109949
Received 3 June 2019; Received in revised form 23 September 2019; Accepted 14 November 2019

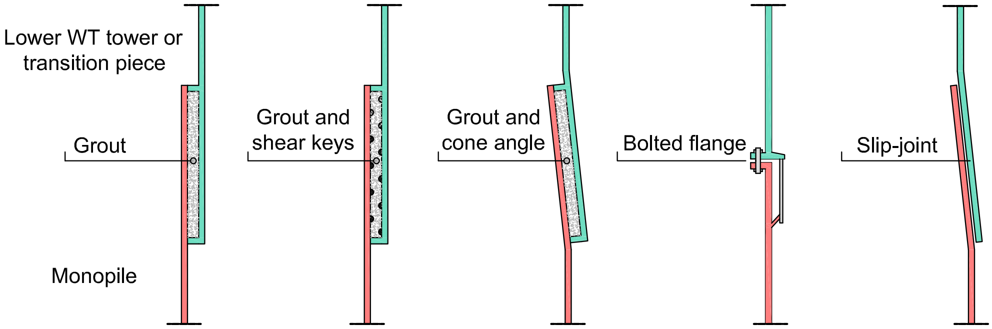

Fig. 1. Schematic layouts of the different connections between the lower wind turbine tower (or transition piece) and the monopile.

Scroby Sands Wind Farm, commissioned in 2004. Afterwards, the bolted flange connection started to be implemented in other offshore wind parks such as the Amrumbank West in the German North Sea, the E.ONs Humber Gateway Wind Farm (UK), the Belwind II in Belgium and the Luchterduinen in the Netherlands [15]. The installation of a bolted connection is faster and more cost-efficient if compared to the grouted connection. However, despite the above mentioned advantages, the bolted connection still needs some special attention in order to be implemented successfully. For example, hammering and driving monopiles with flanges welded on top of the pile could cause possible damage and a decrease of the fatigue resistance of the whole connection. Therefore, not only a high accuracy during hammering is required, but the stresses induced through hammering need to be taken into account in the design phase [16]. A further risk that may affect the structural safety of the connection is related to the sensitiveness of bolts to the highly corrosive offshore environment, calling for further protection in order to ensure their structural longevity. The bolted connection also leads to high maintenance and inspections costs, especially related to the pre-tension aspects of the bolts. Achieving the required bolt tightness is not an easy task, since torque tools may usually lead to 30% deviation of the desired bolt tightness [17]. In order to check the pre-load of the bolts, it is common practice to inspect bolt connections periodically through ultrasonic methods [18] or vibration-based techniques [19]. The Vestas wind turbine collapse in Lemnhult (Sweden), in 2015 [20], is a recent example of structual failure caused by a loss of bolt tightness.

Besides the grouted and bolted connection, a future promising solution is the slip-joint, see Fig. 1. The construction principle of the slip-joint is based on fitting the lower wind turbine tower or the bottom part of the transition piece onto the upper part of the monopile foundation by overlapping two identical conical sections over each other, without the use of bolts, grout or welding. By avoiding the grouting process, not only the transition piece can be built with a smaller diameter, but potentially also the installation time could be substantially reduced. The connection solely depends on the geometry and contact mechanism between the two steel surfaces. Therefore, the load transfer is achieved through the frictional forces between the contact surfaces, which result mainly from the weight of the structure and the overturning moments caused by operational conditions of the wind turbine.

The use of the slip-joint connection for wind turbines was first introduced by WindMaster for their onshore turbines in the 1990s. In 1998 Windmaster went bankrupt and was taken over by Lagerwey, stopping the use of the slip-joint [21]. A connection similar to the slip-joint has been used in the past for onshore turbines by MAN (Maschinenfabrik Augsburg-Nürnberg). The possibility of using the slip-joint for offshore wind turbines was considered only later, in 2003 [21]. Even though the slip-joint technology showed potential benefits back in 2003, it did not lead to the development of any prototypes for offshore use.

1.2. Research scope

At Delft University of Technology, the research on the slip-joint for offshore wind turbines was resumed in 2011 [22,23], when the grouted connection problem became known to the public. Compared to onshore applications, the offshore environment presents a number of new challenges which arise in the design, installation and operational phase of the slip-joint. Among these challenges, the installation technique and the cones imperfections are two factors that need to be taken care of, in order to achieve a sound structural connection. For example, a typical installation approach used for slip-joints in onshore application consists of dropping the upper cone onto the lower cone. The uncontrollable nature of the latter method makes it undesirable for offshore application, since there is a significant risk of damaging the connection and/or the adjacent parts of the monopile. On the other hand, cone imperfections caused by manufacturing tolerances, pile driving or by simple handling manoeuvres, can lead to undesirable localized contact areas increasing the risk of high-stress concentration.

Within this context, the target here is to propose a novel slip-joint installation and decommissioning technique in order to ensure a sound contact during the overlapping and settlement phase between the upper and monopile cone. The proof of concept of the proposed technique is demonstrated by means of a scaled (1:10) experimental slip-joint setup described in Section 2. The key point of the proposed method consists in using an oscillatory force to control the settlement occurrence between the two cones during installation and decommissioning. The results show that an applied oscillatory load with a frequency close enough to one of the natural frequencies of the slip-joint, allows settlement to occur at a chosen forcing frequency. Hammer tests on the testing specimens and experimental modal analysis will provide some insights in relation to which structural modes should be excited in order to effectively obtain a stable settlement. In order to mimic an installation and decommissioning test, the oscillatory excitation covered a frequency range up to 200 Hz for most of the test cases, while for few other tests the frequency range has been increased up to 800 Hz (see Appendix A). The axial load generally varied between − 40 kN (pulling force) and 10 kN (compressive force). Note that few installation tests have also been performed with an axial load up to 60 kN.

The design of the experimental setup and the meausurement program used to demonstrate the proof of concept is described in Section 2. An overview of the vibration-induced settlement results is provided in the first part of Section 3, while more detailed testing results, which mimick the installation and decommissioning procedure, are shown in Sections 3.2–3.5. In Section 4 the results of the experimental modal analysis on the cone-set are shown. Finally, conclusions and a short discussion about ongoing research activities are provided.

1.3. Overview of vibration-induced friction reduction

As mentioned in Section 1.2, the target is to explore the effectiveness of using vibration to reduce friction during the installation and decommissioning phase of a slip-joint. Examples of friction reduction initiated by a vibratory forcing are quite common in engineering applications. For example, the loosening of nuts can be achieved by applying a dynamic forcing; pouring and casting of concrete is often assisted by small shakers to obtain a more homogeneous distribution by facilitating the flow of the material; screw tightening can be improved by ultrasonic vibration; the drivability of foundation piles can also be facilitated by an applied oscillatory force. Since the applications are quite multidisciplinary, a thorough review of vibration-induced friction reduction effects falls outside the scope of this paper. Therefore, a short description of how this topic evolved since the ’60s is provided.

The first experiments highlighting the effect on kinetic and static friction of oscillatory forces have been carried out since the ’60s and ’70s [24–26]. Further experimental results [27] managed to trace down empirical nonlinear relations between the variation of static friction coefficients and the variation in amplitude of the applied oscillatory load. In most of these studies, the coefficients of static friction generally showed decreases between 60 and 80% once a dynamic forcing was applied. A first systematic experimental campaign, in the framework of which either an increase or a decrease in the frictional resistance was achieved by means of changing parameters such as normal force, frequency and amplitude, was performed in the beginning of the ’90s [28]. Concurrently, first analytical solutions, obtained for a Hertzian contact perturbed by a normal oscillation under resonant condition, started to shed some light on vibration-induced friction reduction [29–31]. The results showed that, due to the nonlinear Hertzian stiffness, applied oscillatory forcing causes a reduction of the normal contact deflection resulting in a decrease of the contact area. On average, all the simulations showed a friction force reduction of about 10% [29,31].

A notable work dedicated to bringing tribology and related physics literature to the attention of the controls community has been published in the middle of the ’90s [32]. Various friction compensation techniques were discussed and a thorough review of the application of high-frequency signals (so-called dither signals) immited into a system to modify its frictional behaviour was presented. Later on, the control community focused the attention on how to “silent” or smooth down friction-induced instabilities by exploiting high-frequency excitation [33,34]. Within this context, it is worth mentioning Blekhman’s first attempt to include the subject of vibration-induced friction reduction into one physical and mathematical framework named “vibrorheology” [35].

Despite the variegated applications and extended literature on this subject, a general and clear physical interpretation of the influence of applied vibration on frictional forces is still missing. Quantitative correspondences between proposed models and experimental outcomes within this subject are also quite scarce, even within a laboratory environment. This is mainly due to the lack of knowledge in modelling frictional mechanisms and in its interaction with the system dynamics and applied vibratory forces, which is far from being trivial [36]. Research within this topic is still very active and the target is to pin down possible mechanisms and oscillation properties that could explain the observed frictional behaviour [37,38].

2. Scaled slip-joint setup

2.1. Test setup

To simulate a slip-joint installation and decommissioning procedure considering its self-weight and an applied dynamic load, a test setup was designed that allows for axial loading, relative motion between the cones, and a slight inclination between the longitudinal axes of the cones. A schematic layout and a photograph of the experimental setup are shown in Fig. 2.

For the designed test setup, the cones representing the monopile (MP) and the transition piece (TP) are placed upside down in order to carry out the experiments in a more practical and safer way. The proposed setup allows to excite the TP by means of a shaker located close to the floor. Within this arrangement, the vibrations are applied from the bottom to the TP, whereas the static load is applied at the top cone representing the MP. The H-profile columns, one at each side of the test setup, are connected by mounting plates, thread rod and bolts. Hinges were installed between the load beam and the lateral columns in order to allow a slight tilt of the MP, as indicated in Fig. 2. Possible self-alignment of the cones is facilitated through a couple of ball bearings mounted between the columns and the hydraulic jack, while the machine mounts (rubber bearings) allow the transmission of vibration to the supported TP. The conical shape of these latter mounts provides equal stiffness in the lateral directions and enables a vertical relative motion as well.

2.2. Geometry of the scaled cones

The scaled dimensions of the slip-joint are based on the MP design of the OC3 project [39]. The OC3 project uses an MP of 6 m in diameter with a wall thickness of 60 mm. The desired overlap length for the slip-joint is defined as being the same as for classic grouted connection [21], i.e. 1.5 D_{MP}, where D_{MP} is the diameter of the MP. The cone angle of the TP, β, is chosen smaller than the angle of the conical part of the MP, α. Ideally, this slight difference in cone angle should cause the upper cone to elastically deform during the settlement phase. Therefore, the induced deformation would allow a more uniform contact area to occur. However, due to manufactured cone imperfections, the contact area developed in a non-uniform way after installation. Some further remarks in relation to the contact mechanism are provided later in this section.

The geometric scaling factor S_l for the specimens has been chosen equal to 10. The testing repeatability was checked by using two similar sets of cones. Table 1 shows the scaled dimensions for both sets, cone-set 1 and cone-set 2.

Additional experiments on cone-set 1 have been carried out in order to capture the status of the manufactured cones, since possible geometrical imperfections will most likely influence the contact mechanism between the cones during the experiments. Therefore, a single-point RF603L laser was used to perform measurements of the inner surface of the scaled test specimens. The laser is attached to a small rotating beam located at the centre of the cones, see Fig. 3. The beam is slightly smaller than the radius of the cones, and the laser measures the distance from the laser emitter to the cone surface. The maximum measurable distance is 50 mm, with an accuracy of 0.05 mm. An extendible beam is then used in order to position and fix the laser sensor at a desired axial location inside the cone, see Fig. 3.

The laser then starts to measure, and the beam rotates 370 degrees clockwise, measuring the distance from the laser to the surface of the cone for every degree (the forward loop). The beam then rotates counter-clockwise to the original position, measuring the distances a second time (the backward loop). Rotations of 370 degrees are used to create an overlap in the measurements. This overlap is desirable since it allows to remove the influence of transients at the start and at the end of a measurement. In order to minimize measurement errors, the average of the measured forward loop and backward loop is taken. This process is repeated for chosen axial positions, using steps of 1 to 2 cm. The data has then been interpolated between each measured ring to obtain a more continuous and smoother geometrical representation. The distance measured between the laser and the MP cone inner surface is shown in Fig. 4a, while Fig. 4b presents the top view of the measured deviations obtained by the laser. Note that by plotting the measured laser-cone distance in Fig. 4a and b, both the imperfections and the out-of-roundness of the cone are emphasized and clearly noticeable.

Based on the scanned geometry, a first glimpse of the initial contact and its further development can be obtained. This is accomplished by first aligning the MP and TP axis based on the processed data. The distance between the two sets of data is then manually decreased until

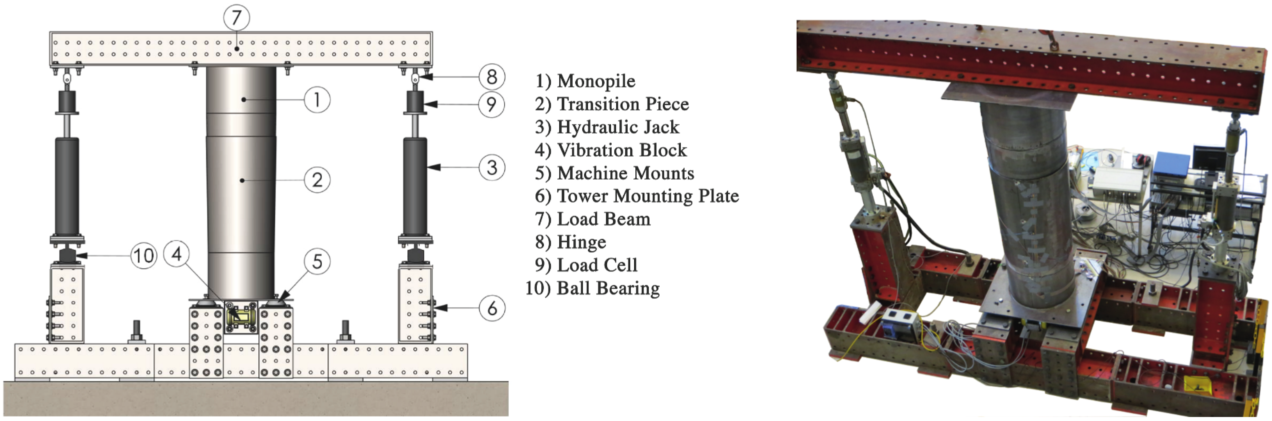

Fig. 2. Experimental setup as built in the Stevinlab at TU Delft.

Table 1
Design parameters of the scaled slip-joint case study.

	MP cone	TP cone	Unit
Cone angle	$\alpha = 1.05$	$\beta = 1.0$	°
Top outer diameter	0.58	0.59	m
Bottom outer diameter	0.60	0.61	m
Wall thickness	6	6	mm
Cone length	1.0	1.0	m
Total length	1.4	1.4	m
Total mass	0.15	0.15	tons
Steel type	S355	S355	

"contact" is established. This occurs when, locally, any of the data points of the MP measurements are equal to or larger than those of the TP. The latter condition is represented in Fig. 5 as a contact distance equal to 0, while the remaining computed distances between the cones have been normalized to the maximum measured distance. The transition from the initial instant of contact to the final settlement between the measured set of cones can be inferred from Fig. 5. The blue lines in the figure represent the longitudinal weld location. Initial contact develops vertically at an overlap of 650 mm. A second contact area is formed by increasing the overlap length to 750 mm. At these two distinct areas, the contact area expands in the circumferential direction once a final overlap of 850 mm is reached.

Fig. 5 shows that a large section of the conical surfaces is not in contact. Note that these plots are based on measurements and no deformation of the cones is taken into account. The local deformation will inevitably increase the contact surface, and the presented final contact status should therefore be considered as a qualitative prediction in order to gain a better understanding of the testing results.

2.3. Sensor layout, static and dynamic loading

Scaling laws need to be derived such that the axial stress σ_{ax} in the scaled setup is similar to the full-scale stress. At first, considering that the gravitational force is related to the volume of the structure, it turns out that the self-weight of the scaled setup and of the full-scale structure is related by a cubic scaling factor S_l^3. Such relation, written in terms of gravitational forces F_g, reads as follows

$$\frac{F_{g,fs}}{F_{g,ms}} = S_l^3 \tag{1}$$

where the subscript "*ms*" stands for model-scale and "*fs*" refers to full-scale. On the other hand, the axial stress σ_{ax} due to a generic applied axial load F_{ax} relates to the cross-section by means of a quadratic scaling factor S_l^2 defined as follows

$$\frac{F_{ax,fs}}{F_{ax,ms}} = \frac{\sigma_{ax} A_{cs,fs}}{\sigma_{ax} A_{cs,ms}} = S_l^2. \tag{2}$$

The mismatch between the two scaling factors has to be compensated by an added axial load F_{add} in order to mimic the axial stress of a full-scale structure. Therefore, the relation that leads to an equivalent axial stress, written in terms of forces, reads as follows

$$F_{g,fs} = S_l^2 (F_{g,ms} + F_{add}). \tag{3}$$

Substituting the term $F_{g,ms}$ in Eq. (3) by using the relation in Eq. (1), the added force can be found according to the following equation

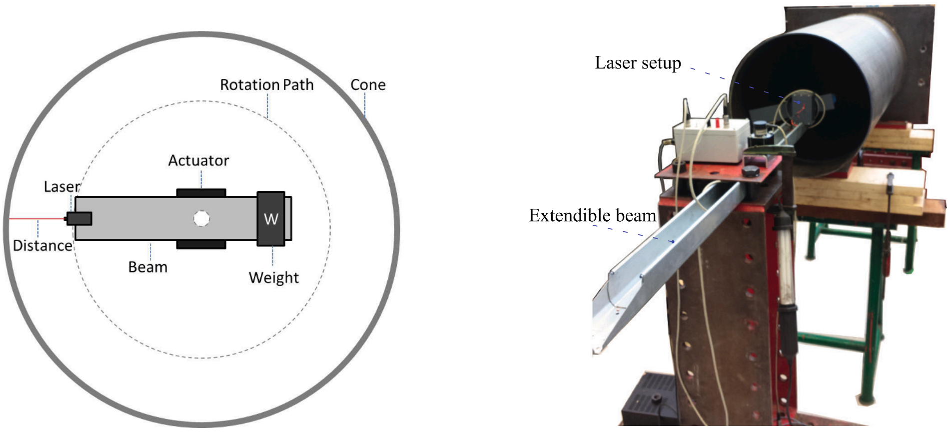

Fig. 3. Laser steup as built in the Stevinlab at TU Delft for the measurement of the inner slip-joint dimensions.

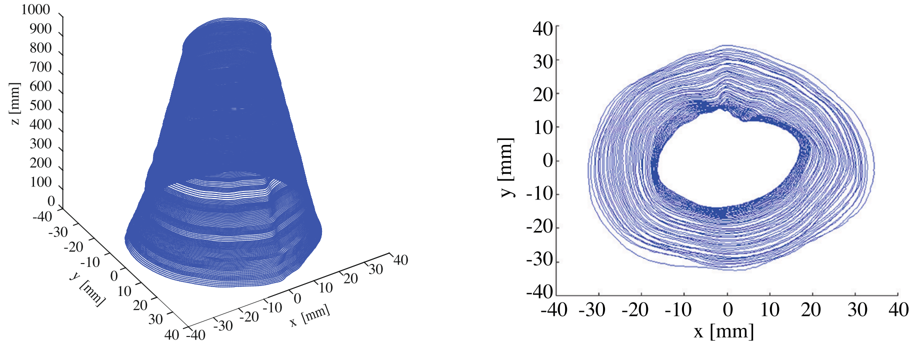

(a) 3D representation of the measured laser–cone distance.

(b) Top view of the measured laser–cone distance.

Fig. 4. Measured out-of-roundness by means of laser scanning of the MP.

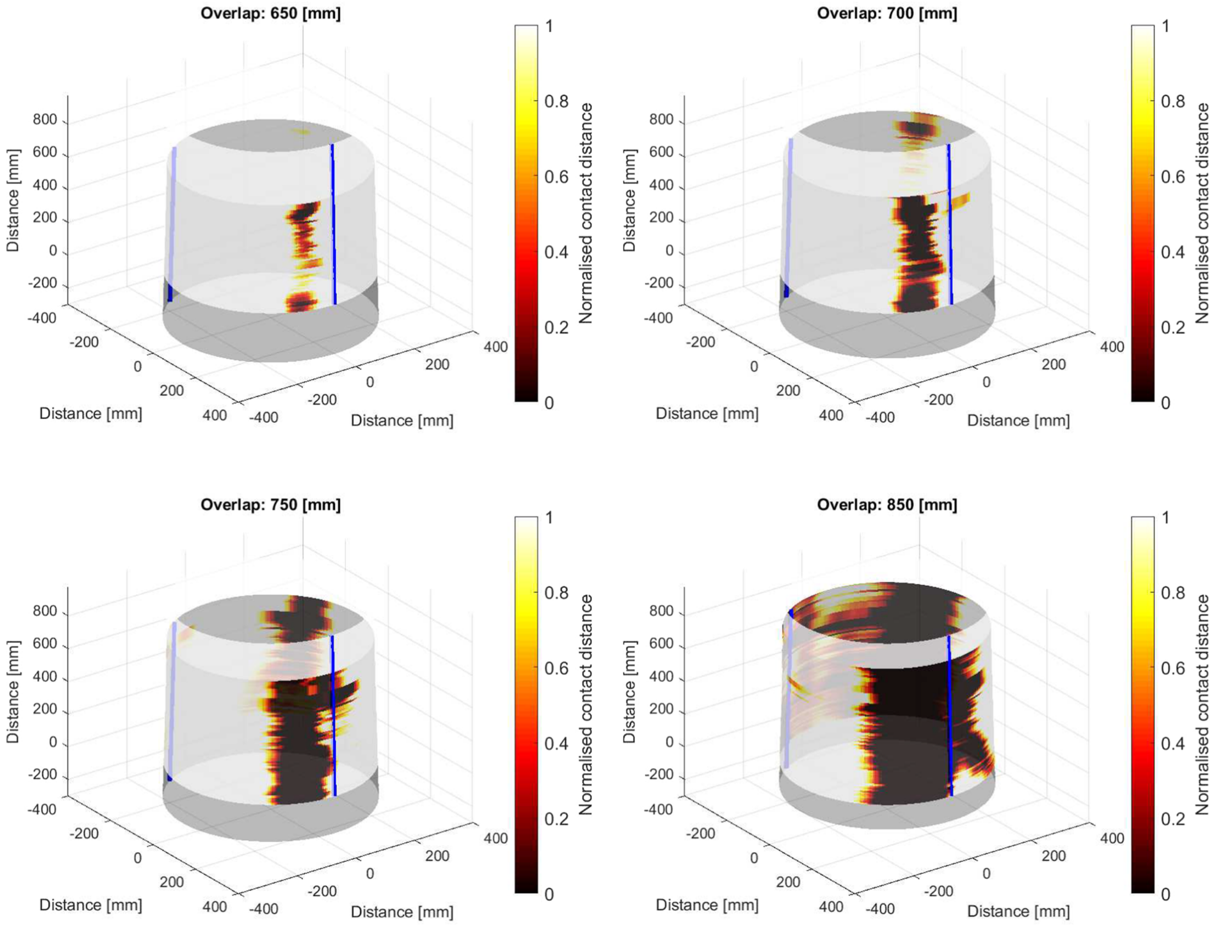

Fig. 5. Contact development as a function of the overlap based on the Laser scanning measurements of the slip-joint.

$$F_{add} = \left(\frac{1}{S_l^2} - \frac{1}{S_l^3}\right) F_{g\,fs}. \tag{4}$$

The additional axial force F_{add}, obtained from Eq. (4), is applied using two hydraulic jacks and is approximately 10 kN. For very few installation tests, see test 9, 39–47, 49, 51–52 in Appendix A and Table 2, such axial load was also increased up to 60 kN.

In order to induce settlement by means of vibration, a harmonic excitation is applied at the TP in either the vertical or horizontal direction. The oscillatory load was applied by two different devices, separately. The first device is an eccentric mass motor, specifically a Wacker NeusonAR 53 (12/250) in combination with a frequency controller from Invertek, which allows the application of high amplitudes. The two motors are mounted at the closed end of the TP, providing a harmonic excitation along the longitudinal/vertical direction of the assembled cones. The second device is an electrodynamic shaker (Bruel & Kjaer type 4812 in combination with a power amplifier type 2707), which allows amplitude control of the input at each frequency. The shaker was laterally connected to the TP with a stiff stinger, see Fig. 6. In order to investigate the influence of the dynamic excitation point on the settlement behaviour of the cone, four different excitation locations were chosen: two excitation points lie close to the bottom, while the other two are located in the middle of the cone. In both cases, the two excitation points have an offset of 90 degrees between each other.

Fig. 7 shows a schematic drawing of the two cones in which the

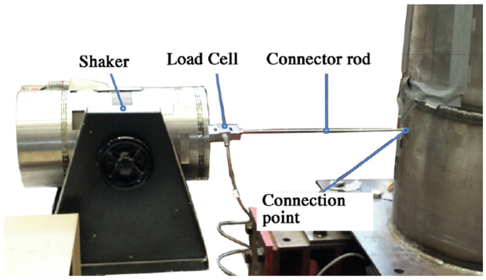

Fig. 6. Electrodynamic shaker connection to one of the four excitation points.

layout of the calibrated sensing devices is indicated. Four displacement sensors (LVDT), which measure distances up to 0.2 m, are equidistantly placed around the circumference. These are used to measure and provide a final averaged displacement that occurs during the installation and dismount experiments. Two strain gauge setups have been used, a first one for cone-set 1 and a more dense sensor grid for cone-set 2. The sensitivity of the strain gauges is about 0.1 µm and a sampling frequency of 2 kHz was used. The layout for cone-set 1 consists of four instrumented sections located at different heights, on the inside of the MP and outside part of the TP. Each section contains three strain gauges. A strain gauge named MP4S3 indicates a sensor placed on the MP at section MP4 and with a string number 3. For cone-set 2, the strain gauges are placed at three different heights and section on the outside part of the TP. For the latter case, the position of a strain gauge is denoted with a string location (S) and a height location (H), where the height position is measured with reference to the open end of the TP. At each instrumented section, a ring of eight equally spaced strain gauges are placed, measuring strains in the circumferential direction. In reference to Fig. 7, the strain gauge H10S2 refers to the sensor located at 10 cm from the open end of the TP and at the circumferential position of string 2.

2.4. Measurement program and test cases

The experimental setup is used to simulate installation and decommissioning tests. The following main installation sequence is performed:

1. Lower the MP onto the TP under self-weight;
2. Simulate the full-scale self-weight;
3. Apply a dynamic load with a stepwise or linear increase of frequency.

Step 3 is the key point of the installation test, during which an oscillatory loading is applied and its frequency is increased in either small steps of maximum 5 Hz or by a constant increment. In the experiments where a stepwise increment of the frequency is applied, the frequency is kept constant at the instance when settlement occurs. The frequency is increased further only after the settlement has stopped/stabilized. On the other hand, during the experiments where the frequency increased constantly, various rates of frequency increment were used. Besides installation, also the decommissioning test of the slip-joint has been carried out. For the latter case, the oscillatory load is applied after the application of a pulling force. Therefore, by changing the loading frequency, the frequencies that provide the most efficient dismount of the cones can be identified. For the decommissioning experiments, the following steps are used:

1. Initiate a pulling force that is similar in magnitude as step 2 of the installation test;
2. Apply a dynamic load with a stepwise or linear increase of frequency, until the upper cone disconnects.

In total 77 tests were performed on two sets of cones, focusing on either the installation or the dismount of the cones. In Appendix A, Tables 2 and 3, a summary of the different batches of these experiments is provided. In Section 4, the most significant testing results are highlighted and discussed in order to illustrate the proof of concept of the proposed installation and decommissioning technique.

3. Slip-joint installation and decommissioning experiments

3.1. Highlights and discussion of results

Appendix A lists all the testing cases that have been carried out on the two sets of cones. As outlined by Tables 2 and 3, the tests have been classified in different batches from 1 to 6, for both installation and decommissioning tests, and for two different cone-set. For the majority of the test cases (installation and decommissioning), the frequency range during which a final effective settlement occurred turned out to

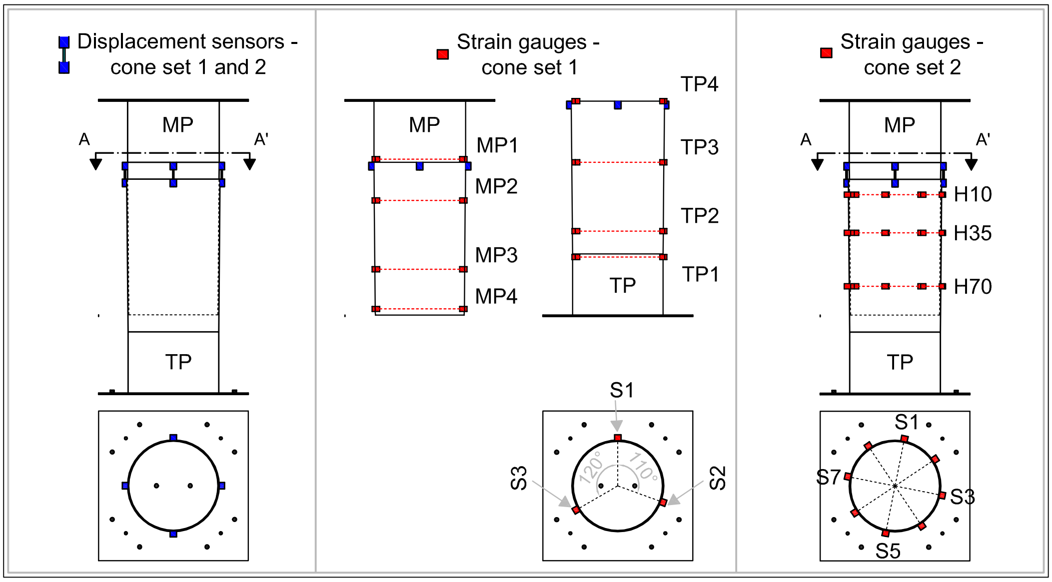

Fig. 7. Sensor layout on the cones during the experiments. The left figure shows the layout of the displacement sensors, while the figure in the middle and the right one show the strain gauge layout for cone-set 1 and cone-set 2, respectively.

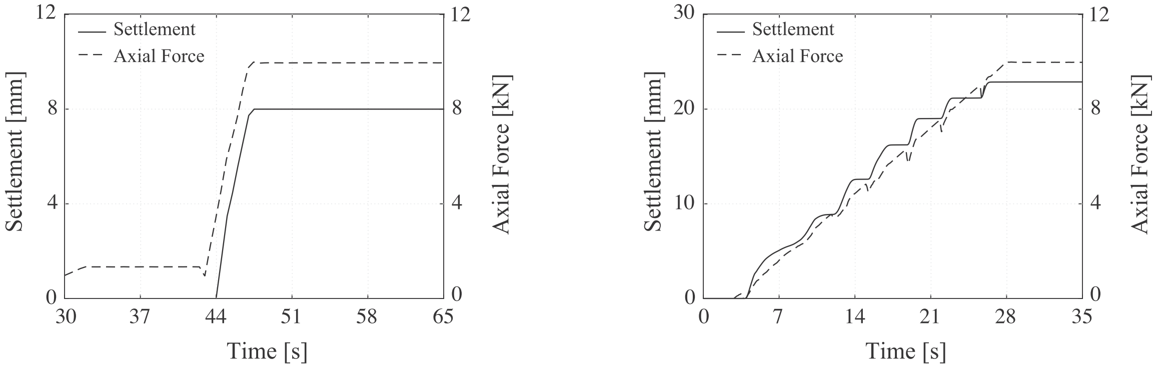

(a) Large increment of the self-weight, Test 20.

(b) Small increment of the self-weight, Test 71.

Fig. 8. Settlement achieved as a result of the simulated self-weight.

be between 119 Hz and 126 Hz, even though smaller settlements during the installation step have been observed at lower excitation frequencies. Furthermore, few decommissioning tests (test 48, 50 and 53, see Appendix A and Table 3) were carried out at frequencies up to 300 Hz, and a dismount has been observed at 249 Hz as well.

Batch 1 refers to the initial installation and dismounting experiments carried out with cone-set 1. These first tests immediately showed that the application of an oscillatory force at certain frequencies facilitates the settling between the cones and that a larger applied static compressive or pulling force does not necessarily lead to larger settlements. Note that several attempts were required to successfully dismount the cones for the first time. A pulling force of −40 kN and a dynamic force at 85 Hz allowed a first successful dismount. After these first tests, the experimental setup was improved by adding ball bearings underneath the hydraulic jacks in order to allow the self-alignments between the cones.

The experiments carried out for batch 2 successfully reproduced the observation that large settlements occur only while specific frequencies of the slip-joint are excited. The axial capacity of the slip-joint was also tested with a maximum compressive force up to 60 kN. The latter load is a scaled force simulating the weight provided by a fully installed wind turbine tower and rotor-nacelle assembly. Somewhat surprisingly, no additional settlement was observed, proving that installing the slip-joint with an assisted vibratory force provides the joint with sufficient axial capacity to bear the turbine height. Subsequently, the dependency on the frequency increment during dynamic tests have been checked for cone-set 1 (batch 2) and cone-set 2 (batch 3). If a large incremental frequency step is used during the dynamic tests, the effective resonance frequencies, which allow large settlements to occur, can be overshot. Therefore, missing certain resonant frequencies prevents a full slip-joint settlement to occur. The test results suggest that a final settlement depth needs time to develop and a small incremental frequency is therefore recommended.

During batch 4, the eccentric motors were replaced by an electrodynamic shaker in order to perform controlled-amplitude tests. Despite the smaller vibration amplitude provided by the electrodynamic shaker (50 to 250 times lower than to the amplitude provided by the eccentric motors), and the different direction of applied harmonic forcing, the same stick-settlement-stick behaviour occurred whenever certain resonance frequencies were excited. This difference in dynamic force magnitude and direction and the similarities of the stick-settlement-stick pattern, clearly demonstrated that the frequency of vibration is the dominant factor that enables settlements to occur. In addition, the settlement behaviour did not vary by changing the location and direction of the applied vibratory load, be it horizontal or vertical. However, it is worth remarking that the final settlements obtained by means of the electrodynamic shaker in batch 4 are slightly smaller than the ones provided by the eccentric motors. This could be attributed to the change of forcing direction (from vertical to lateral), or to the lower dynamic loading amplitude provided by the electrodynamic shaker which may increase the frictional resistance, even though there is no clear evidence of that since various factors such as wear and possible deformations of the cones after repetitive testing could have had an influence on the settlement. Note that some observations found in literature may support the hypothesis of increasing frictional resistance as soon the dynamic load amplitude decreases. For example, Paslay and Plunkett [40] showed through experiments performed on shrink fitted steel cylinders that the static coefficient of friction between rough surfaces drops off with increased normal pressure. In the following years, similar experimental observations have been provided by other authors as well [41,26,42,43], even though no consensus has been found about the physical mechanism triggering the observed phenomenon. Archard [41], for example, attributed the friction dropping mechanism at higher loading amplitude to an increase of the contact surface if elastic theory is obeyed, while Nolle [26] suggested that plastic deformation may play a more important role. On the other hand, Etsion [43] links the increase of static friction to the adhesion force which becomes more predominant at lower normal loads.

The electrodynamic shaker was also used for the experiments carried out on cone-set 1 (batch 5). Again, the results indicated that several resonant frequencies turned out to be effective for triggering significant settlement events. In line with the results provided by batch 4, the final settlement depths were generally lower than the ones achieved in batch 1 and 2 by using the eccentric motors for comparable static compressive forces. The eccentric motors have been used again for the tests performed in batch 6 in order to confirm the settlement behaviour of cone-set 1 observed in batch 1 and 2.

In the following subsections, a summary of the results obtained during the experiments is illustrated in order to back up the previous discussion.

3.2. Static load installation tests

Fig. 8 presents both the relative settlement and the axial load applied to simulate the self-weight of the upper cone. The plots show that small increments of the applied static axial force play a role in the observed settlement behaviour of the joint. When a slow increase in the axial force is applied, Fig. 8b, a stick-slip settlement behaviour is immediately observed. The measured displacements varied between individual incremental tests. Specifically, the observed settlement decreases with an increase in the number of increments. Note that these results highlight that the various settlements, obtained by either a large or small variation of the static loads, occur in an uncontrolled and unpredictable manner. It will be shown that frequency-driven tests enable to control the time at which a settlement/dismount event will occur during the installation and decommissioning test.

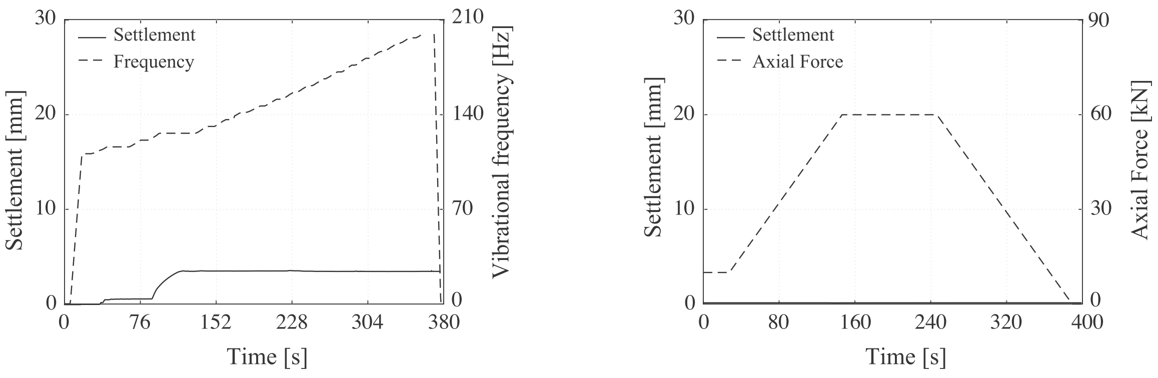

(a) Slow step wise frequency increase, Test 8.

(b) Slip-joint capacity static test, Test 9.

Fig. 9. Load bearing capacity test of the slip-joint.

A further static test was performed in order to check whether the slip-joint was able to carry the simulated weight of an assembled turbine tower. Therefore, once a stable settlement has been achieved through the vibration-assisted installation procedure, Fig. 9a, an additional static load up to 60 kN has been applied on top of the slip-joint. Note that Fig. 9a only shows the final part of the vibration-assisted installation tests performed with a static load of 10 kN, and previous settlements occurred at lower loading frequencies. Fig. 9b shows the applied axial force and the measured relative settlement of the upper cone. Even though the applied axial force is a sixfold increase if compared to the applied axial load for the vibration-assisted installation tests, no further settlement was observed.

3.3. Frequency-driven installation tests

In Fig. 10a, the relative settlement between the cones and the excitation frequency as a function of time is shown with a step-wise increase in frequency for test 1. The settlement occurs only at a number of specific frequencies. At each of these frequencies, the settlement first increases and then stabilizes at a certain level. Concerning test 1, Fig. 10b also shows the static axial force applied by the hydraulic jacks and the amplitude of the vibratory force over time. Both figures indicate that, although the amplitude of the dynamic force keeps increasing, settlement only occurs in several instances. After the last settlement event, achieved at frequency of 110 Hz (at approximately 380 s), the amplitude of vibration tripled at 200 Hz. The absence of any settlement after a frequency of 110 Hz demonstrates that the settlement process is mainly driven by the excitation frequency.

The results of an installation test during which a vibration with an incremental frequency variation of 2 Hz/s are presented in Fig. 11a. For small frequency increments, the settlement slowly persists after hitting the target frequency of 120 Hz, eventually reaching a final stick condition. Fig. 11b, in contrast, shows the results for an increment of the increase in frequency of 10 Hz/s. This increment was varied to investigate the time dependence of the settlement process. Comparing both plots, it can be observed that a final sticking condition is only reached when the settlement is given sufficient time to develop. Therefore, if the effective frequencies are passed rapidly, uncontrolled settlements may occur in time (see Fig. 11b at 380 s). For the sake of clarity, Fig. 11 is obtained from two different sets of cones. The recorded absolute settlement levels differ from test to test, as nulling of the sensors was performed at different positions from the start of the individual tests.

For the first installation experiments with the electric shaker (batch 4), frequencies up to 800 Hz were applied in order to identify the effective settlement frequencies higher than 120 Hz. The results show that the most effective frequencies in the two sets of cones were found at approximately 120 Hz for both sets, and additionally around 249 Hz for cone-set 2, see Fig. 12a. This shows that more effective resonance frequencies that allow vibration-assisted settlements between the cones are present, even though the most significant settlements all occur within the operational frequency range between 0 and 200 Hz. For the sake of completeness, a detailed example of “high” frequency-induced settlement is given in Fig. 12b. For test 52, an axial force of 28 kN and a constant forcing frequency of 249 Hz were used. The amplitude of the dynamic force was increased in a step-wise manner. Fig. 12b shows that each of the first four amplitude steps triggered a settlement event, with a total settlement of 4 mm. Each settlement event temporary stabilized after a short time period. After the fourth step, the additional increase of the amplitude had no significant effect. These results suggest that

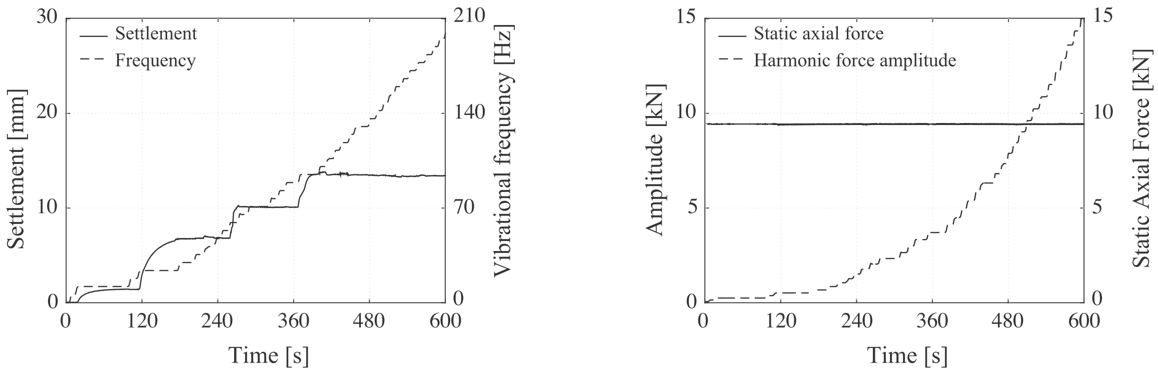

(a) The settlement of the upper cone and the vibrational frequency, Test 1.

(b) The applied dynamic and static force, Test 1.

Fig. 10. The settlement of the upper cone as a function of the vibrational frequency and the applied forces over time.

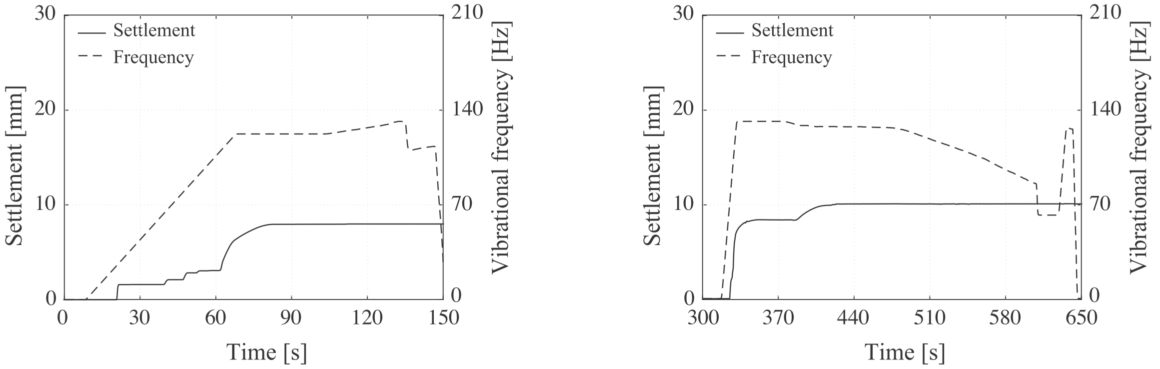

(a) Increment in frequency of 2 Hz/s, Test 75.

(b) Increment in frequency of 10 Hz/s, Test 16.

Fig. 11. Measured settlements and excitation frequencies over time for different frequency increments of the dynamic load.

settlement occurrence, at a specific resonance frequency, could be controllable by the applied vibratory forcing amplitude and that the settlement stabilizes after each event.

Generally, all the installation tests show comparable frequency-driven settlement patterns. Small differences were found in the frequencies that were identified to be effective for each set of cones. For example, for test 12 on cone-set 2 in Fig. 13a, distinct settlements were observed at forcing frequencies of 30, 54, 86, 110, 115 and 126 Hz. On the other hand, Fig. 13b shows the results of test 72 carried out on cone-set 1, where settlement events seem to occur at 27, 78, 110, 115 and 120 Hz. These differences may originate from the manufacturing tolerances which certainly affects the geometry and the symmetry of the two cone sets and therefore the development of the contact mechanism.

3.4. Strains induced during installation

Fig. 14 shows the circumferential strains at the ring of gauges at MP2, MP4, TP2 and TP4 obtained during installation test 1 (see Fig. 10). In order to clearly visualize the settlement occurrence, the displacements shown in Fig. 10a are shown in both plots through a red dashed line. The negative and positive signs define a compressive and tensile behaviour, respectively. The out-of-roundness spotted by means of the laser scanning measurements (see Figs. 4,5), clearly reflects on the measured strains. For example, given that the TP cone angle is slightly larger than the MP cone angle, one would expect to observe a larger compressive strain at section MP2, where most of the load transfer should take place. However, the measured compressive strains seem to be higher at section MP4. On the other hand, the measured strains on the TP suggest that parts of the circumference are expanding, while other parts are in compression. A uniform and symmetric contact between two perfectly cylindrical rings would result in a uniform extension/strain value around the circumference. A similar behaviour was observed in test 12 and test 16, for cone-set 2, where a larger grid of sensors have been installed on the TP (see Fig. 15). It is interesting to note that in Fig. 15b the vibratory load was applied with a certain delay, and the starting point is marked by the dashed grey line. The dynamic force was then rapidly increased from 0 to 132 Hz within 15 s, during which the settlement changed abruptly from approximately 12 mm to 20 mm. Subsequently, the frequency was lowered to 127 Hz with smaller frequency decrements, leading to an additional settlement of 2–3 mm.

As mentioned above, this non-uniform contact can be explained by the result of the measured geometry of cone-set 1 and the qualitative prediction of the contact based on these measurements (see Section 2.2). The measurements of the individual cones indicated that the cones are far from being perfectly conical. As highlighted in Fig. 5, the contact between the two cones develops at two distinct areas and expands in the circumferential direction with an increase in settlement. The simulated contact mechanism is observed to be asymmetric, which may explain the strains measured around the circumference during the installation experiments.

It is worth mentioning, that the observed strain levels are well within the elastic region which lies at approximately 1600 microstrains for S355 steel. The resulting strain levels show that no yielding of the material occurred during the vibration-assisted installation of the slip-joint.

3.5. Frequency-driven decommissioning tests

Fig. 16a and b show the settlements and excitation frequencies of tests 15 and 76, representing the results of two types of decommissioning tests where the dynamic force has been applied by the

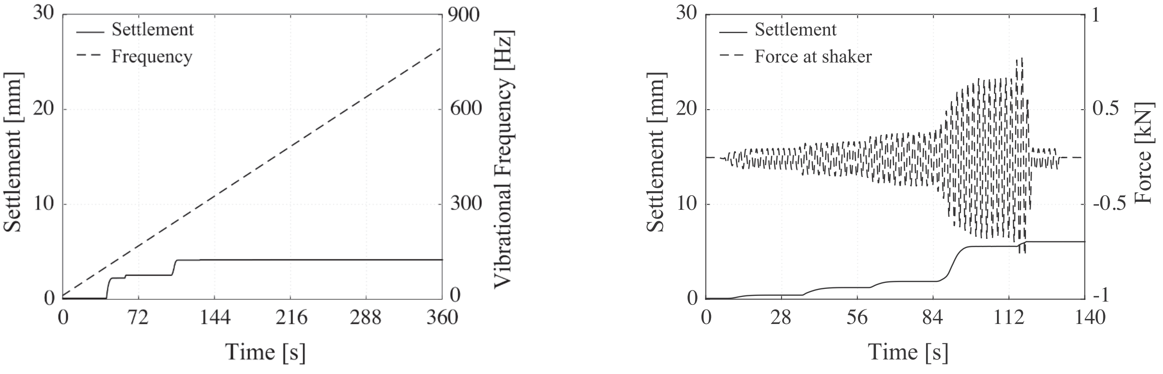

(a) Excitation frequency and displacements, Test 41.

(b) Shaker force and displacements, Test 52.

Fig. 12. Measured settlements obtained from the electrodynamic shaker.

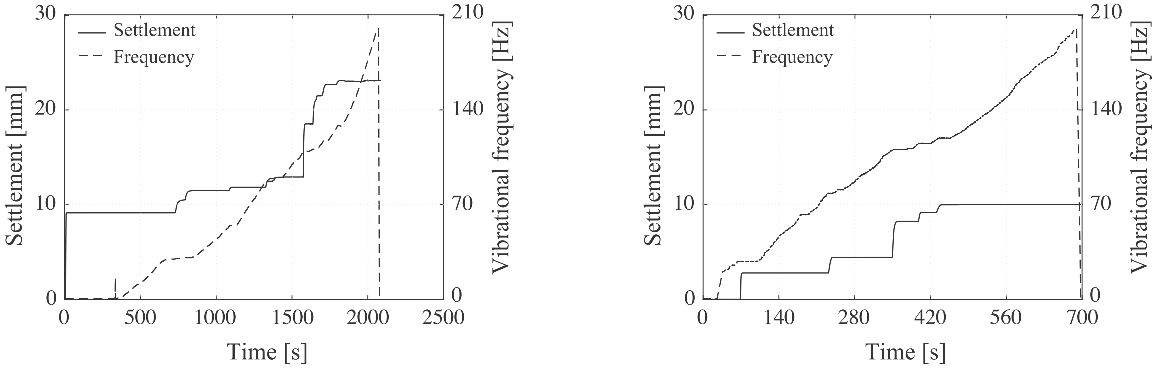

(a) Excitation frequency and displacements, Test 12.

(b) Excitation frequency and displacements, Test 72.

Fig. 13. Measured settlements of the upper cone and applied forcing frequency on cone-set 1 and cone-set 2.

eccentric motors. Fig. 16a refers to a dismount test carried out by stepwise increasing the excitation frequency. On the other hand, Fig. 16b shows the results of a frequency ramp-up test. For both tests, a pulling force of −30 kN and −22 kN, respectively, have been applied in order to allow the separation of the two cones. Similar results can be retrieved by both types of tests, meaning that the cones separate at a frequency of approximately 120 Hz.

Fig. 16b also shows the time dependence of the vibration-assisted decommissioning. As soon the excitation frequency reaches 120 Hz, the cone starts to move, but a settling time is needed before completing the full separation. This again confirms the previous observation, made in Section 3.3, where it has been shown that the duration of the applied oscillatory load influences the sliding event. The necessary pulling force in order to assist the vibration-based decommissioning ranged between −15 kN and −30 kN, whenever an oscillatory load around 120 Hz (or 249 Hz for few test cases) is applied. Note that, the −15 kN magnitude is similar to the self-weight of the transition piece, indicating that, on full-scale, the same lifting equipment used for installation could be used for the decommissioning phase.

Most of the attempts to dismount the cones with lower frequencies than 120 Hz turned out to be unsuccessful unless a higher pulling force was used. For example, in order to dismount the cones by ramping the forcing frequency up to 85 Hz during test 7, an axial static force of −40 kN was required. This confirms the importance of frequency band around 120 Hz for the installation and decommissioning phase for the investigated slip-joint setup. Similar results have been obtained by using the electric shaker. As mentioned in Section 3.1, for few decommissioning tests, an additional settlement frequency was also found at 249 Hz. Overall, for dismounting purposes, an electric shaker seems to be as effective as the eccentric motors.

4. Experimental modal analysis

4.1. Overview

So far, the results of multiple installation tests showed that the majority of settlements occur at frequencies of approximately 80 Hz, 105 Hz, and 120 Hz, while further settlements were observed around 30 Hz, 51–55 Hz, 90–95 Hz and 108–115 Hz. Specifically, frequencies nearby 120 Hz seem to be effective for both the installation and dismounting of the cones, regardless of the different amplitude of the vibratory load provided by the two shaking devices. For the sake of completeness, settlements also occurred at higher frequencies such as 135 Hz, 193 Hz and 249 Hz. In order to check the correspondence of these “settlement frequencies” with the resonance frequencies of the test setup, an experimental modal analysis has been carried out of cone-set 1 in its final stick position. The next sections describe the measurement method, the test setup, the processing of the collected data, the resulting frequency response functions, and the identified mode shapes of the test setup.

4.2. Test setup

Experimental modal analysis was performed by using the roving sensor method [44]. An impact hammer (ICP 086D05) in combination with PCB Piezotronics’ high sensitivity (1000 mV/g) tri-axial accelerometers (ICP 356B18) were used to generate and measure the dynamic responses, respectively. The raw data has been recorded at 10 kHz and the generated impulse allowed to sufficiently excite frequencies up to 2–2.5 kHz. Since the main “settlement frequencies” were observed in a frequency range between 0–200 Hz, the data was

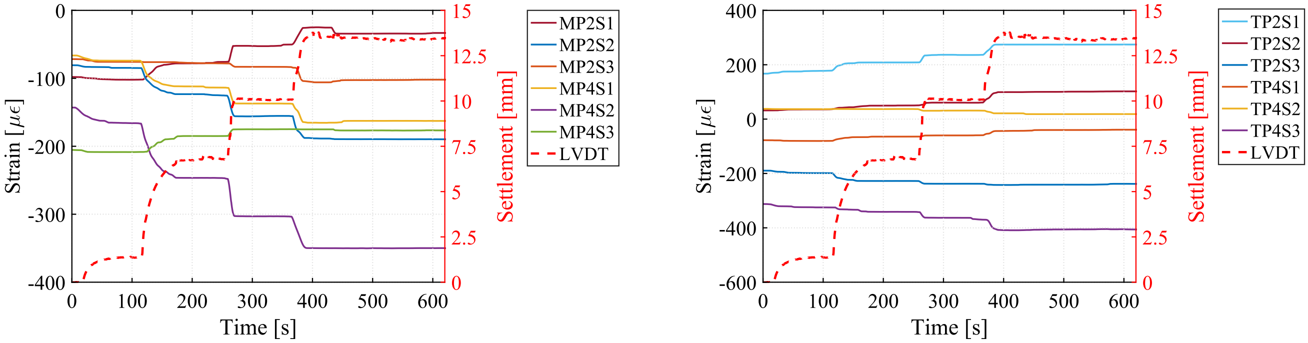

(a) Installation test 1 on cone-set 1, MP.

(b) Installation test 1 on cone-set 1, TP.

Fig. 14. Measured circumferential strains (a) on the monopile and (b) on the transition piece of cone-set 1 during test 1. The dashed red line refers to the measured settlements. The labelling refers to the sensor layout shown in Fig. 7. (For interpretation of the references to colour in this figure legend, the reader is referred to the web version of this article.)

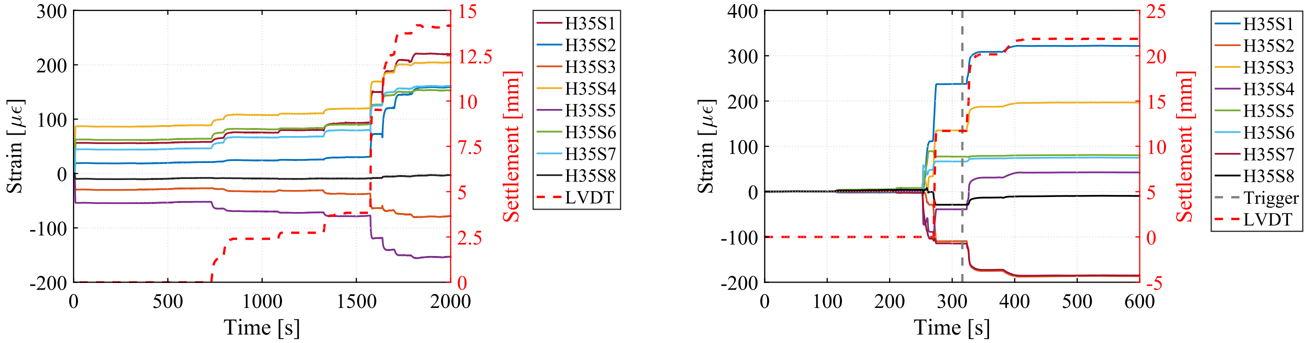

(a) Installation test 12 on cone-set 2, TP.

(b) Installation test 16 on cone-set 2, TP.

Fig. 15. Measured circumferential strains on the transition piece of cone-set 2 during test 12 (a) and test 16 (b). The dashed red line refers to the measured settlements. In (b), the grey dashed line indicates the time instant when the vibratory load was applied. The labelling refers to the sensor layout shown in Fig. 7. (For interpretation of the references to colour in this figure legend, the reader is referred to the web version of this article.)

subsequently low-pass filtered to 0.8 kHz and downsampled to 1 kHz. Each individual impact is simultaneously measured by five accelerometers. Fig. 17 shows the chosen sensing grid: in total, 80 points along the outer slip-joint surface are measured, while impacts are applied in two directions with an angle difference of 90 degrees; 5 different cross-sections have been measured at different heights, while the dynamic response of each cross-section was captured through 16 equally spaced measurement points. To accurately capture the dynamic behaviour of the chosen cone area, the five sensors were relocated around the surface after five impacts for each input location. The data acquisition system used for the modal tests is a Mueller-BBM-Vas' PAK MKII.

4.3. Modal identification and comparison with observed settlements

The sensor data for each setup are acquired in local coordinates. To create a single model of the structure, the data is therefore first converted to a global coordinate system. Frequency response functions (FRFs) were computed from the hammer pulses and the free decay structural responses. The quality of each FRF was checked by inspecting its corresponding coherence function. Subsequently, the modal properties such as frequencies, damping and mode shapes were identified by an automated version of the Eigensystem Realization Algorithm (ERA), see [45], in order to combine the results of 16 different measurement setups. Given that ERA is a parametric system identification method, a model order needs to be chosen. However, the choice of a model order can be by-passed through the use of stabilization charts, which allow to check the convergence of identified modal properties by increasing model orders. The inspection and interpretation of the stabilization diagram have been automated by means of a system pole clustering method [46], which allows to automatically recognize, select, sort and group the stable modal features. The stabilization diagram has been constructed by running the identification algorithm with a model order range of 40–90 with an increasing step of 2, while the Hankel matrix is built by means of a lag value equal to 300 (see [45] for further details concerning the ERA input parameters).

Fig. 18a provides an example of the modulus of 32 estimated FRFs at section H1, while Fig. 18b shows 32 FRSs estimated over the last measured circumferential section H5. The blue vertical dots form the stabilization diagram retrieved from the ERA results. The modal properties such as frequency, damping and mode shape are then obtained by averaging all the modal features obtained for the identified poles (represented by the blue dots) corresponding to a vertical "frequency" line [46].

A first inspection of the results shows that the resonance peaks below 70 Hz seem to be quite scattered and very low in amplitude. Conversely, at frequencies between 110 and 170 Hz the resonances exhibit sharp and distinct peaks. Considering the low amplitude of the peaks, it is most likely that the recorded cone-set dynamics in both frequency bands is significantly affected by the structural response of the whole experimental setup. As mentioned earlier, the hammer test was performed on the mounted cone-set in order to capture the dynamic behaviour of the installation test. Hammer tests on a free-free boundary cone-set would reveal different resonance frequencies compared to the ones observed during the installation and decommissioning tests. On the other hand, in the frequency band between 70 and 110 Hz, the cone-set dynamic is characterized by two main modal bells which most likely refer to the cross-sectional modes of the cone-set. These two

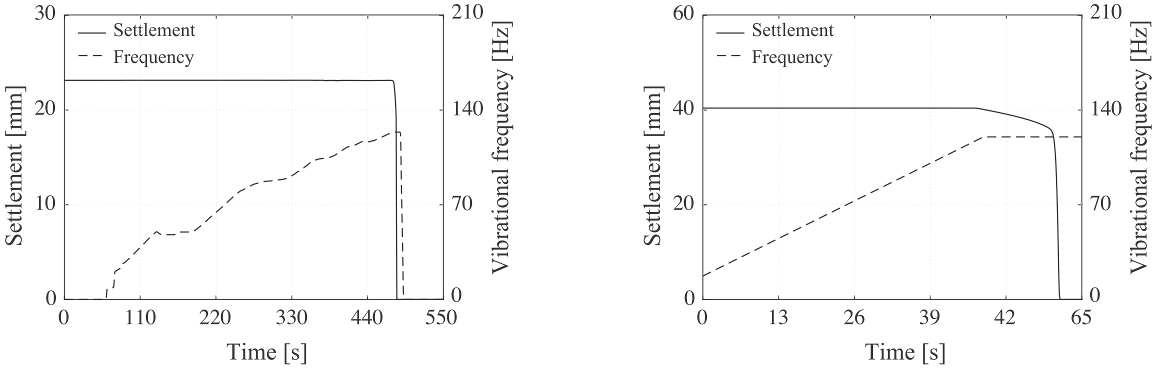

(a) Step-wise increase, Test 15.

(b) Constant increase, Test 76.

Fig. 16. Displacement of the upper cone for dismount tests using eccentric motors and applying different methods of increasing the frequency of vibration up to 120 Hz in combination with a pulling force of 15 kN.

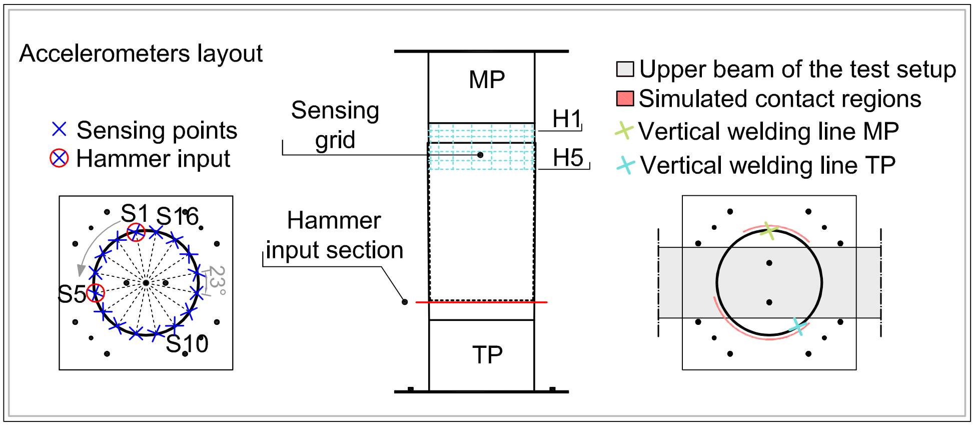

Fig. 17. Layout of the accelerometers installed on the test setup for experimental modal analysis. The left figure shows the circumferential sensing grid, the figure in the middle displays a schematic view of the vertical sensing points of the chosen slip-joint surface, and the right figure highlights the cone-set orientation compared to the upper beam and the location of the vertical welding lines. The cross makers refer to sensing and hitting location, while the black dots are a schematic representation of the bolts location. (For interpretation of the references to colour in this figure legend, the reader is referred to the web version of this article.)

distinct modal bells repeat themselves with a frequency step of ≈100 Hz. A noticeable feature of the resonances between 80 and 110 Hz is the splitting phenomenon of the peaks. Even though this phenomenon needs still to be investigated in further details, its origin is most likely due to the boundary conditions (cone-set attached to the ground and to the upper beam) and the break of symmetry of the cone-set.

Fig. 19 shows a short list of the mode shapes identified between 0 and 140 Hz. For clarity, shell vibration modes are characterized here by a circumferential node line n. The first two identified modes at 5.6 Hz and at 20 Hz (Fig. 19a-b) seem to be a combination of bending motion along the North-West and South-West direction, respectively, and the first cross-sectional circumferential mode, $n = 1$. The three mode shapes between 26 and 45 Hz (Fig. 19c-e), resemble the second cross-sectional circumferential mode, $n = 2$. Moderate torsional motion can be observed at 55.9 Hz (Fig. 19f), while a more pronounced one has been identified at 62.8 Hz (Fig. 19g). The third cross-sectional circumferential mode, $n = 3$, shows up between 83 and 87 Hz (Fig. 19h-i). As mentioned earlier, the modal bell in that narrow frequency range exhibit a splitting phenomenon of the resonance peak. At 105 Hz, the mode shape still tends to resemble the third circumferential mode, however the motion seems to be affected by bending towards the North-East direction (Fig. 19j). The source of the bending mechanism observed in some mode shapes could be explained by the boundary conditions of the cone-set, especially by the lateral dynamics of the upper beam combined with the lateral hydraulic jacks. Note that the mode shapes do not show any discontinuity at the transition from the lower cone to the upper cone. This observation demonstrates that the cones act as a bonded system.

The identified mode shape at 120 Hz (Fig. 19k) seems to exhibit a dynamic motion along the North-West-South-East direction, while on the diametrically opposed direction the cone seems to stay quite steady. As suggested by the scanning laser measurement in Section 2.2, two opposed sides of the cone-set seem to be more prone in developing a contact mechanism due to the out-of-roundness of the cone-set. These regiones are marked in Fig. 17 with a red arc. Therefore, a possible explanation of the observed motion is that the areas that are in contact may exhibit a higher local stiffness compared to the areas that are not in contact. Note that the mode at 120 Hz proved to be one of the most effective ones for both installation and decommissioning tests. The last identified mode at 130.4 Hz (Fig. 19l) shows a circumferential node line $n = 4$.

In general, most of the “settlement frequencies” correspond well with the identified mode shapes and their corresponding frequencies. This correspondence proves that the identified mode shapes, which reflect the cone dynamics combined with the dynamics of the whole test setup, do have an effect on settlement behaviour. Note that for the settlements observed within the frequency range of 90–95 Hz, no mode shapes were identified. This can be due to identification problems, since during the hammer tests carried out only on the combined cones the eventual mode may have not been excited.

5. Discussion and conclusions

A proof of concept for a new method for installing and dismounting a slip-joint has been investigated from an experimental perspective. The proposed technique has been illustrated by means of a 1:10 slip-joint scaled model, and consists in applying a vibratory load to the upper part of the joint in order to facilitate a sound settlement between the two cones. The results of the installation and decommissioning tests demonstrate that selecting the right forcing frequency is the key for a successful installation/dismount of a slip-joint. The experiments showed that the deliberate excitation of some resonance frequencies of the slip joint is found to be effective in order to achieve a sound structural connection. The settlements of the cones tend to stabilize in

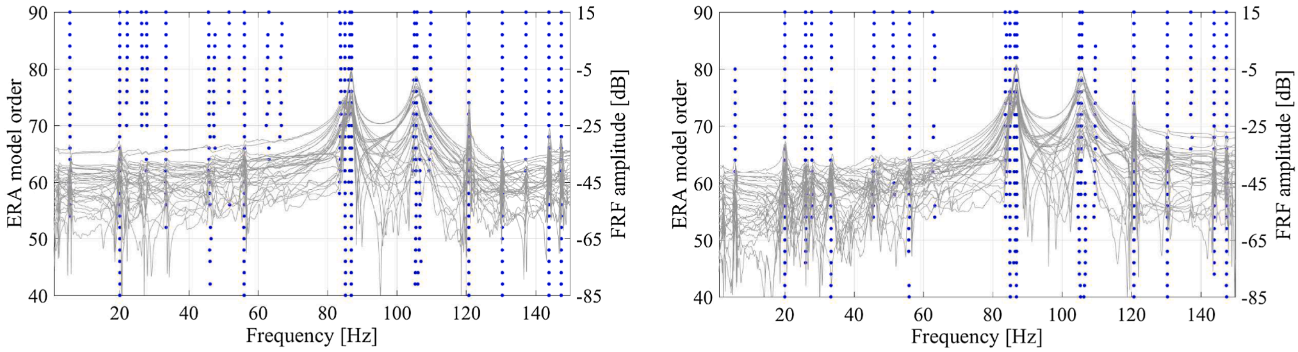

(a) FRFs and ERA results, section H1.

(b) FRFs and ERA results, section H5.

Fig. 18. Frequency response functions and ERA stabilization charts.

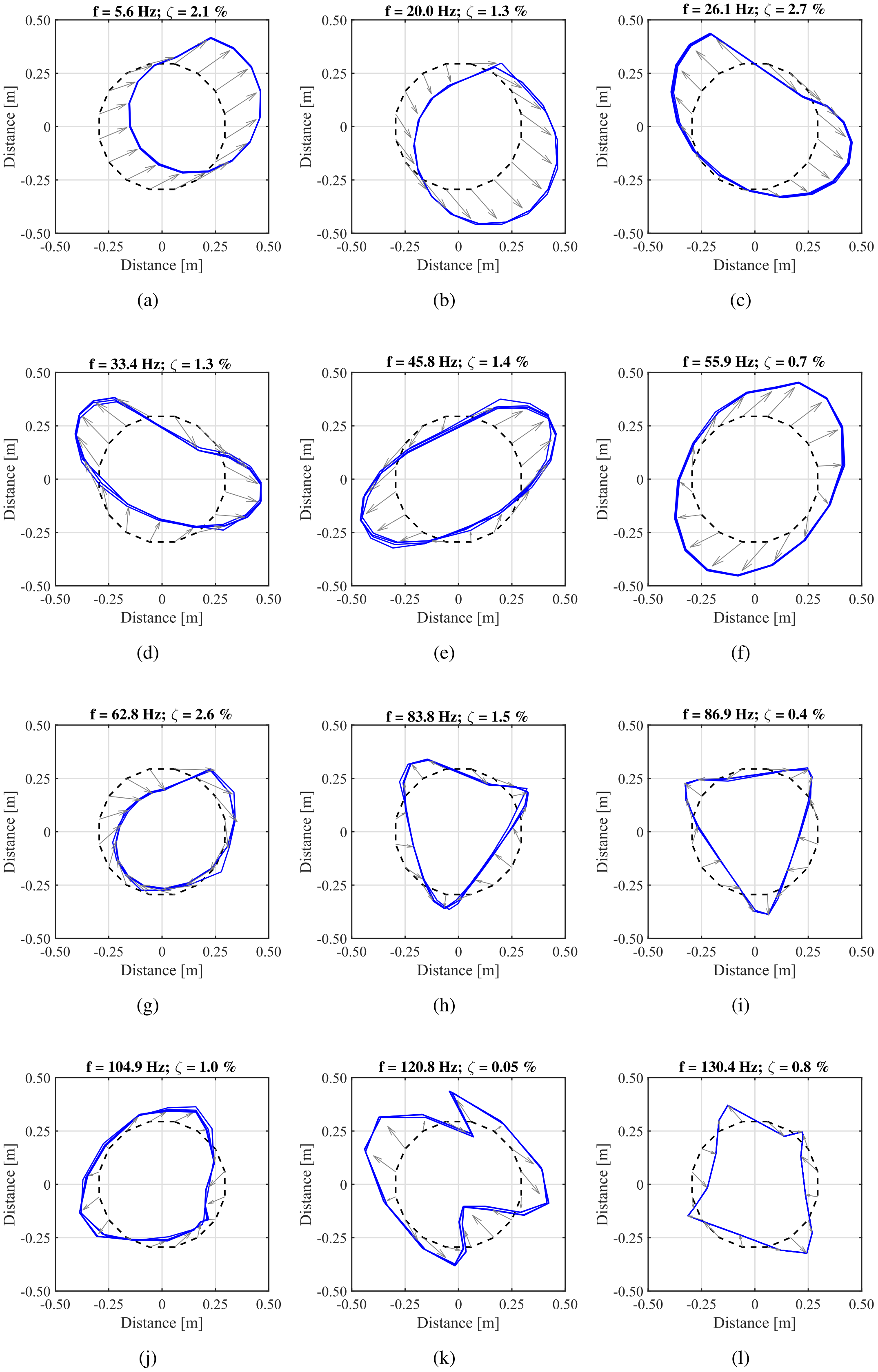

Fig. 19. Identified mode shapes from ERA. The black dashed line indicates the undeformed cone, while the blue lines refer to the mode shapes. The grey arrows define the direction of motion of each measured point. The North and South directions refer to the top and bottom part of each plot, respectively. For the colored plots, please refer to the online version of the manuscript.

time showing that a sound contact can be achieved by means of the proposed vibration-assisted installation technique.

Specifically, it was observed that a sound contact between the two cones was achieved by using relatively small frequency increments, and final settlements were mostly observed between a frequency range of 119–126 Hz for the installation tests. On the other hand, when the increment of the frequency is too large, only a partial settlement can be achieved. The large frequency increment provides a shorter settling time, preventing the occurrence of a stable connection. The tests also demonstrated that the method of a linear increase in the frequency of vibration leads to similar settlement levels as the tests performed with a stepwise frequency increase, provided that a relatively small increment of the frequency is used. The advantage of linearly increasing the frequency of vibration lies in its simplicity and could therefore be an option for actual full-scale implementation. The decommissioning tests showed that the cones could be dismounted most effectively when vibrating at a frequency around 120 Hz, and for few test cases at a frequency of 249 Hz.

The use of the electric shaker allowed to investigate the influence of the applied vibration amplitude, to check the effectiveness of “settlement” and “decommissioning” frequencies up to 800 Hz, and the direction of dynamic forcing. The results of these tests showed that a similar settlement behaviour is obtained with a dynamic forcing amplitude 50 to 250 times smaller than that provided by the eccentric motor. Most importantly, the electric shaker tests also highlighted that even though settlement events are mainly initiated by the forcing frequency, it was observed a few times that settlement occurrence at a specific forcing frequency could be controlled by the amplitude of the oscillatory forcing. However, future research is needed on this matter, in order to assess whether or not the proposed method can be extended towards a fully controllable technique. A further advantage of using the electric shaker is given by the limited amount of force required, which makes this technique suitable for on-site application. The tested system seemed also to be unaffected by the direction of the applied vibratory load, which would facilitate practical applications. To such regard, research activities concerning the application of the proposed herein new vibration-assisted method to decommission a prototype slip-joint installed in an offshore environment are already ongoing. Therefore, the final target is to investigate which modes, if excited, are most suitable to facilitate the decommissioning of an installed slip-joint and to quantify the reduction of the pulling force when a vibratory load is applied.

Besides the successfull testing results, some open points still remain and are currently under investigation. The strain measurements, for example, showed a non-uniform deformation around the circumference, indicating a non-uniform contact. This non-uniform contact can be explained by the result of the measured irregular geometry of the cones of set 1 and the prediction of the contact based on these measurements. It seems clear that manufacturing error and tollerances will play a significant role in developing a reliable model of the slip-joint. A numerical model is going to be developed in order to assess the influence of the non-uniform contact on the stress and dynamic behaviour of the tested cones. In general, the findings of the described experiment will also help to validate the numerical model of the slip-joint, which may shed some light on the sensitivity of other factors for the contact area development and for the settlement mechanism. Within a long-term perspective, it is worth highlighting the research directions required to fully assess the slip-joint technology. In terms of designing the slip-joint and predicting its lifetime structural capacity the following aspects need further investigations: (a) scaling effects; (b) contact development in time and robustness with respect to manufacturing tolerances, operational and environmental conditions; (c) fretting problems of the slip-joint. On top of that, there is scope to further improve the installation and decomissioning method. The one proposed herein, leverages on the fact that the vibration-induced friction reduction may be more effective if only certain modes are excited. However, in order to speed up the method, it may be worth assessing and comparing the performance between applied random vibration and single frequency dynamic forcing.

Declaration of Competing Interest

The authors declare that they have no known competing financial interests or personal relationships that could have appeared to influence the work reported in this paper.

Acknowledgements

The work was part of the Slip Joint Offshore Research project (ref. TEHE116334-SJOR). The authors would like to thank Kees van Beek and John Hermsen from the Stevinlab of the Faculty of Civil Engineering and Geosciences at TU Delft, for their crucial contribution in constructing the experimental setup, and for the assistance during testing. A further acknowledgement goes to Siamand Rahimi, former member of the Railway Engineering group at TU Delft, for the support during the hammer tests, and to Koen Hermans for the initial assistance in designing the two cone setups. At last, the authors are thankful to Dr. Eliz-Mari Lourens for providing constructive feedback on the first complete version of the manuscript.

Appendix A

See Tables 2 and 3.

Table 2
Overview of the installation test setup and final settlement.

Nr.	Batch	Set	Device	Frequency increase	Axial force [kN]	Final settlement
1	1	1	Ecc. Motor	Step-wise incr. to 200 Hz	10	13.4 mm
8	2	1	Ecc. Motor	Step-wise incr. to 200 Hz	10	12 mm
9	2	1	only axial force		10–60	No settlement
11	2	1	Ecc. Motor	Linear incr. to 128 Hz in 13 s	10	11 mm
12	3	2	Ecc. Motor	Slow step-wise incr. to 200 Hz	10	14 mm
14	3	2	Ecc. Motor	Slow step-wise incr. to 200 Hz	10	11.5 mm
16	3	2	Ecc. Motor	Linear incr. to 130 Hz in 15 s	10	10 mm
18	3	2	Ecc. Motor	Linear incr. to 126 Hz in 13 s	10	13 mm
20	3	2	Ecc. Motor	Linear incr. to 126 Hz in 13 s	10	9.8 mm
22	3	2	Ecc. Motor	Slow step-wise incr. to 200 Hz	10	11.4 mm
24	3	2	Ecc. Motor	Slow step-wise incr. to 200 Hz	10	10.7 mm
26	3	2	Ecc. Motor	Linear incr. to 125 Hz in 26 s	10	12.5 mm
28	3	2	Ecc. Motor	Linear incr. to 125 Hz in 60 s	10	11.3 mm

(*continued on next page*)

Table 2 (*continued*)

Nr.	Batch	Set	Device	Frequency increase	Axial force [kN]	Final settlement
30	3	2	Ecc. Motor	Step-wise incr. to 130 Hz	10	11.2 mm
32	3	2	Ecc. Motor	Linear incr. to 130 Hz	10	10 mm
35	3	2	Ecc. Motor	Step-wise incr. to 193 Hz	10	7.55 mm
36–37	3	2	Ecc. Motor	Linear incr. to 123 Hz	10	12.7 mm
39–40	4	2	E.D. shaker (low pos.)	Sweep 20–400 Hz in 180 s	18	3 mm
41	4	2	E.D. shaker (low pos.)	Sweep 20–800 Hz in 600 s	20	3.9 mm
42–44	4	2	E.D. shaker (low pos.)	Sweep 20–250 Hz in 230 s	20	No settlement
45–47	4	2	E.D. shaker (low pos.)	Sweep 20–250 Hz in 230 s	24	2.2 mm
49	4	2	E.D. shaker (low pos.)	249 Hz, ampl. step-wise incr.	28	10 mm
51	4	2	E.D. shaker (high pos.)	Sweep 20–300–249.5 Hz in 280 s	32	1.5 mm
52	4	2	E.D. shaker (high pos.)	249 Hz, ampl. step-wise incr.	28	6 mm
54	5	1	E.D. shaker (high pos.)	Step-wise between 20 and 400 Hz	10	8.5 mm
56	5	1	E.D. shaker (high pos.)	Step-wise between 119 and 200 Hz	10	7.1 mm
57	5	1	E.D. shaker (low pos.)	Sweep 20–320 Hz with 1 Hz/s	10	at 240 Hz 1 μm
59	5	1	E.D. shaker (low pos.)	Step-wise incr. up to 300 Hz	10	4.7 mm
61	5	1	E.D. shaker (low pos.)	Shaking at 120 Hz	10	7 mm
63	5	1	E.D. shaker (low pos.)	Step-wise incr. up to 300 Hz	10	3 mm
65	5	1	E.D. shaker (low pos.)	Shaking at 120 Hz	10	4.6 mm
67	5	1	E.D. shaker (high pos.)	Shaking at various frequencies	10	10 mm
69	5	1	E.D. shaker (high pos.)	Shaking at 260 Hz and 120 Hz	10	6 mm
71	6	1	only axial force		0–10 kN in 20 s	Stick-slip
72	6	1	Ecc. Motor	Step-wise incr. to 200 Hz	10	10 mm
75	6	1	Ecc. Motor	Slow ramp up to 120 Hz in 60 s	10.	7.9 mm
77	6	1	Ecc. Motor	Slow ramp up to 120 Hz in 200 s	10	8.5 mm

Table 3
Overview of the decommissioning test setup and final disconnection.

Nr.	Batch	Set	Device	Frequency increase	Axial force [kN]	Disconnection
2–6	1	1	Ecc. Motor	Various linear incr.	−6, −10, −15, −20	no dismount
7	1	1	Ecc. Motor	Step-wise incr. up to 85 Hz	−40	Successful
10	2	1	Ecc. Motor	Step-wise incr. up to 128 Hz	−30	Successful
13	3	2	Ecc. Motor	Slow step-wise incr. up to 128 Hz	−30	Successful
15	3	2	Ecc. Motor	Slow step-wise incr. up to 127.5 Hz	−30	Successful
17	3	2	Ecc. Motor	Linear incr. up to 126 Hz in 13 s	−30	Successful
19	3	2	Ecc. Motor	Linear incr. up to 124 Hz in 13 s	−30	Successful
21	3	2	Ecc. Motor	Linear incr. up to 127 Hz in 13 s	0 to −30	Successful
23	3	2	Ecc. Motor	Linear incr. up to 125 Hz	0 to −30 to −35	Successful
25	3	2	Ecc. Motor	Linear incr. up to 125 Hz in 13 s	0 to −30	Successful
27	3	2	Ecc. Motor	Linear incr. up to 125 Hz in 60 s	−20	Successful
29	3	2	Ecc. Motor	Linear incr. up to 120 Hz in 60 s	−20	Successful
31	3	2	Ecc. Motor	Linear incr. up to 120 Hz in 60 s	−20	Successful
33–1:2	3	2	Ecc. Motor	Linear incr. up to 118 Hz; 128–116 Hz	−18	Successful
34	3	2	Ecc. Motor	Linear incr. up to 118 Hz	−20	Successful
38	3	2	Ecc. Motor	Linear incr. up to 118 Hz	10 to −30	Successful
48	4	2	E.D. shaker (low pos.)	Sweep 230–250 Hz	−27	Successful
50	4	2	E.D. shaker (low pos.)	Shaking at 249 Hz	−28 to −30	Successful
53	5	1	E.D. shaker (high pos.)	Sweep 20–300 Hz with 1 Hz/s	24 to −34	Successful
55	5	1	E.D. shaker (high pos.)	Step-wise up to 119 Hz	−30	Successful
58	5	1	E.D. shaker (low pos.)	Shaking at 119 Hz	−30	Successful
60	5	1	E.D. shaker (low pos.)	Shaking at 119 Hz	−24	Successful
62	5	1	E.D. shaker (low pos.)	Shaking at 120 Hz	−24	Successful
64	5	1	E.D. shaker (low pos.)	Shaking at 120 Hz	−20	Successful
66	5	1	E.D. shaker (high pos.)	Shaking at 120 Hz	−30	Successful
68	5	1	E.D. shaker (high pos.)	Shaking at 120 Hz	−20 to −40	Successful
70	6	1	Ecc. Motor	Linear incr. up to 118 Hz	−20 to −30	Successful
73	6	1	Ecc. Motor	Linear incr. up to 118 Hz	−24	Successful
74	6	1	Ecc. Motor	Linear incr. up to 118 Hz	−22	Successful
76	6	1	Ecc. Motor	Linear incr. up to 118 Hz	−22	Successful

References

[1] de Vries E. Offshore monopile failure – a solution may be in sight. Wind Power Month Mag 2010https://www.windpowermonthly.com/article/1011507.

[2] NoordzeeWind, Operations report 2009, Technical Report, NoordzeeWind; 2010. <http://www.noordzeewind.nl/wp-content/uploads/2012/02/OWEZ_R_000_20101112_Operations_2009.pdf>.

[3] DNV, Joint industry project summary report from the JIP on the capacity of the grouted connections in offshore wind turbine structures, Technical Report 2010-1053, Det Norske Veritas AS; 2011a.

[4] Lotsberg I, Serednicki A, Lervik A, Bertnes H. Design of grouted connections for monopile offshore structures. Stahlbau 2012;81(9):695–704. https://doi.org/10.1002/stab.201201598.

[5] Dallyn P, El-Hamalawi A, Palmeri A, Knight R. Experimental testing of grouted connections for offshore substructures: a critical review. Structures 2015;3:90–108. https://doi.org/10.1016/j.istruc.2015.03.005.

[6] Dallyn P, El-Hamalawi A, Palmeri A, Knight R. Experimental investigation on the development of wear in grouted connections for offshore wind turbine generators. Eng Struct 2016;113:89–102. https://doi.org/10.1016/j.engstruct.2015.11.028.

[7] Lee J-H, Won D-H, Jeong Y-J, Kim S-H, Kang Y-J. Interfacial shear behavior of a high-strength pile to sleeve grouted connection. Eng Struct 2017;151:704–23. https://doi.org/10.1016/j.engstruct.2017.08.035.

[8] Chen T, Xia Z, Wang X, Zhao Q, Yuan G, Liu J. Experimental study on grouted

connections under static lateral loading with various axial load ratios. Eng Struct 2018;176:801–11. https://doi.org/10.1016/j.engstruct.2018.09.056.

[9] DNV, Design of offshore wind turbine structures, Technical Report DNV-OS-J101, Det Norske Veritas AS; 2011.

[10] Voßbeck M, Löhning T, Kelm M. Structural behaviour of grouted connections for monopile foundations of offshore wind turbines. Stahlbau 2013;82(1):55–60. https://doi.org/10.1002/stab.201301652.

[11] Fehling E, Leutbecher T, Ismail M, Schmidt M. Grouted connections of offshore wind energy plants. Part 2: Modeling and design. Stahlbau 2014;83(Suppl. 2):46–60. https://doi.org/10.1002/stab.201430007.

[12] Tziavos N, Hemida H, Metje N, Baniotopoulos C. Non-linear finite element analysis of grouted connections for offshore monopile wind turbines. Ocean Eng 2019;171:633–45. https://doi.org/10.1016/j.oceaneng.2018.11.005.

[13] Lotsberg I. Structural mechanics for design of grouted connections in monopile wind turbine structures. Mar Struct 2013;32:113–35. https://doi.org/10.1016/j.marstruc.2013.03.001.

[14] Njomo-Wandji W, Natarajan A, Dimitrov N. Probabilistic structural assessment of conical grouted joint using numerical modelling. Ocean Eng 2018;158:232–52. https://doi.org/10.1016/j.oceaneng.2018.03.089.

[15] Gollub P, Jensen JF, Giese D, Güres S. Flanged foundation connection of the Offshore Wind Farm Amrumbank West: Concept, approval, design, tests and installation. Stahlbau 2014;83(8):522–8. https://doi.org/10.1002/stab.201410178.

[16] Jensen KS, Petersen SJ, Pedersen RR. European offshore wind engineering – past, present and future. Proc Inst Civil Eng – Civil Eng 2018;171(4):159–65. https://doi.org/10.1680/jcien.17.00040.

[17] Bickford J. An introduction to the design and behavior of bolted joints. 4th ed. Boca Raton, Florida, USA: CRC Press Taylor & Francis Group; 2008.

[18] Chaki S, Cornelup G, Lillamand I, Walaszek H. Combination of longitudinal and transverse ultrasonic waves for in situ control of the tightening of bolts. J Pressure Vessel Technol 2006;129:383–90. https://doi.org/10.1115/1.2748821.

[19] Sah SM, Thomsen JJ, Brøns M, Fidlin A, Tcherniak D. Estimating bolt tightness using transverse natural frequencies. J Sound Vib 2018;431:137–49. https://doi.org/10.1016/j.jsv.2018.05.040.

[20] SHK, Olycka med vindkraftverk i Lemnhult, Vetlanda kommun, Jönköpings län, den 24 december 2015, Technical Report RO 2017:01, Swedish Accident Investigation Authority; 2017.

[21] van der Tempel J, Schipholt BL. The slip-joint connection, alternative connection between pile and tower, Technical Report F1W2-JvdT-03-093/01-P, Dutch Offshore Wind Energy Converter (DOWEC). NL: Delft University of Technology; 2003.

[22] Segeren MLA, Hermans KW. Experimental investigation of the dynamic installation of a slip-joint connection between the monopile and tower of an offshore wind turbine. J Phys: Conf Ser 2014;524:012080. https://doi.org/10.1088/1742-6596/524/1/012080.

[23] Segeren MLA, Lourens E, Tsouvalas A, Van Der Zee TJJ. Investigation of a slip-joint connection between the monopile and the tower of an offshore wind turbine. IET Renew Power Gener 2014;8:422–32.

[24] Fridman HD, Levesque P. Reduction of static friction by sonic vibrations. J Appl Phys 1959;30(10):1572–5. https://doi.org/10.1063/1.1735002.

[25] Tolstoi D. Significance of the normal degree of freedom and natural normal vibrations in contact friction. Wear 1967;10(3):199–213. https://doi.org/10.1016/0043-1648(67)90004-X.

[26] Nolle H, Richardson R. Static friction coefficients for mechanical and structural joints. Wear 1974;28(1):1–13. https://doi.org/10.1016/0043-1648(74)90097-0.

[27] Broniec Z, Lenkiewicz W. Static friction processes under dynamic loads and vibration. Wear 1982;80(3):261–71. https://doi.org/10.1016/0043-1648(82)90254-X.

[28] Skåre T, Ståhl J-E. Static and dynamic friction processes under the influence of external vibrations. Wear 1992;154(1):177–92. https://doi.org/10.1016/0043-1648(92)90253-5.

[29] Hess DP, Soom A. Normal vibrations and friction under harmonic loads: Part i–Hertzian contacts. J Tribol 1991;113(1):80–6. https://doi.org/10.1115/1.2920607.

[30] Hess DP, Soom A. Normal vibrations and friction under harmonic loads: Part ii–rough planar contacts. J Tribol 1991;113(1):87–92. https://doi.org/10.1115/1.2920608.

[31] Hess DP, Soom A, Kim C. Normal vibrations and friction at a Hertzian contact under random excitation: Theory and experiments. J Sound Vib 1992;153(3):491–508. https://doi.org/10.1016/0022-460X(92)90378-B.

[32] Armstrong-Hélouvry B, Dupont P, Canudas De Wit C. A survey of models, analysis tools and compensation methods for the control of machines with friction. Automatica 1994;30(7):1083–138. https://doi.org/10.1016/0005-1098(94)90209-7.

[33] Thomsen JJ. Using fast vibrations to quench friction-induced oscillations. J Sound Vib 1999;228(5):1079–102. https://doi.org/10.1006/jsvi.1999.2460.

[34] Thomsen JJ. Some general effects of strong high-frequency excitation: Stiffening, biasing and smoothening. J Sound Vib 2002;253(4):807–31. https://doi.org/10.1006/jsvi.2001.4036.

[35] Blekhman II. Vibrational mechanics – nonlinear dynamic effects, general approach, applications. Singapore: World Scientific; 2000.

[36] Cabboi A, Woodhouse J. Validation of a constitutive law for friction-induced vibration under different wear conditions. Wear 2018;396–397:107–25. https://doi.org/10.1016/j.wear.2017.08.010.

[37] Popov M, Popov VL, Popov NV. Reduction of friction by normal oscillations. I. Influence of contact stiffness. Friction 2017;5(1):45–55. https://doi.org/10.1007/s40544-016-0136-4.

[38] Mao X, Popov VL, Starcevic J, Popov M. Reduction of friction by normal oscillations. II. In-plane system dynamics. Friction 2017;5(2):194–206. https://doi.org/10.1007/s40544-017-0146-x.

[39] Jonkman J, Musial W. Offshore code comparison collaboration (OC3) for IEA task 23 offshore wind technology and deployment, Technical Report NREL/TP-5000-48191. Golden, CO, USA: National Renewable Energy Laboratory; 2010.

[40] Paslay P, Plunkett R. Design of shrink-fits. Trans ASME 1953;75:1199–202.

[41] Archard J. Single contacts and multiple encounters. J Appl Phys 1961;32:1420–5. https://doi.org/10.1063/1.1728372.

[42] Rabinowicz E. The tribology of magnetic recording systems – an overview. Tribol Mech Magnetic Storage Syst 1986;3:1–7.

[43] Etsion I, Amit M. The effect of small normal loads on the static friction coefficient for very smooth surfaces. J Tribol 1993;115(3):406–11. https://doi.org/10.1115/1.2921651.

[44] Ewins DJ. Modal testing: theory, practice, and application. 2nd ed. Hertfordshire, England: Baldock; 2000.

[45] Juang JN, Pappa RS. An eigensystem realization algorithm for modal parameter identification and model reduction. J Guid, Control Dyn 1985;8(5):620–7. https://doi.org/10.2514/3.20031.

[46] Cabboi A, Magalhães F, Gentile C, Cunha Á. Automated modal identification and tracking: application to an iron arch bridge. Struct Control Health Monitor 2017;24(1):e1854. https://doi.org/10.1002/stc.1854.